A&A 443, 133–141 (2005)
DOI: 10.1051/0004-6361:20053587


Astronomy & Astrophysics

# The contribution of rotational velocity to the FP of elliptical galaxies

A. Riciputi[1], B. Lanzoni[2], S. Bonoli[3], and L. Ciotti[1]

[1] Dipartimento di Astronomia, Università di Bologna, via Ranzani 1, 40127 Bologna, Italy
e-mail: andrea.riciputi@bo.astro.it
[2] INAF – Osservatorio Astronomico di Bologna, via Ranzani 1, 40127 Bologna, Italy
[3] Department of Astronomy & Astrophysics, University of Toronto, 60 St. George Street, Toronto, ON, M5S 3H8, Canada

Received 7 June 2005/ Accepted 28 July 2005

**ABSTRACT**

The contribution of ordered rotation to the observed tilt and thickness of the Fundamental Plane of elliptical galaxies is studied by means of oblate, two-integrals cuspy galaxy models with adjustable flattening, variable amount of ordered rotational support, and possible presence of a dark matter halo and of a central super-massive black hole. We find that, when restricting the measure of the velocity dispersion to the central galactic regions, rotation has a negligible effect, and so cannot be responsible of the observed tilt. However, streaming velocity effect can be significant when observing small and rotationally supported galaxies through large (relative) aperture (as for example in Fundamental Plane studies at high redshift), and can lead to unrealistically low mass-to-light ratios. The effect of a central supermassive black hole on the kinematical fields, and the models position in the $v/\sigma$-ellipticity plane are also discussed.

**Key words.** galaxies: elliptical and lenticular, cD – galaxies: fundamental parameters – galaxies: photometry – galaxies: kinematics and dynamics

## 1. Introduction

In the observational three-dimensional space of central velocity dispersion $\sigma_0$, (circularized) effective radius $R_e$, and mean surface brightness within the effective radius $I_e = L/(2\pi R_e^2)$ (where $L$ is the total galaxy luminosity), early-type galaxies approximately locate on a plane, called the Fundamental Plane (hereafter FP; Dressler et al. 1987; Djorgovski & Davis 1987), and represented by the best-fit relation:

$$\log R_e = a \log \sigma_0 + b \log I_e + c. \quad (1)$$

The coefficients $a$, $b$, and $c$ depend slightly on the considered photometric band (e.g., Pahre et al. 1998; Scodeggio et al. 1998): for example, by measuring $R_e$ in kpc, $\sigma_0$ in km s$^{-1}$, and $I_e$ in $L_\odot/\mathrm{pc}^2$, reported values in the Gunn r band are $a = 1.24 \pm 0.07$, $b = -0.82 \pm 0.02$, $c = 0.182$[1] (Jørgensen et al. 1996, hereafter JFK). One of the most striking observational properties of the FP is its small and nearly constant thickness: the distribution of $\log R_e$ around the best-fit FP (at fixed $\sigma_0$ and $I_e$) has a measured *rms* (hereafter $\sigma_{\rm int}$) corresponding to a scatter in $R_e \sim 15\% \div 20\%$ (after correction for measurement errors, see, e.g., Faber et al. 1987; JFK).

[1] This value of $c$ refers to the Coma cluster and to $H_0 = 50$ km s$^{-1}$ Mpc$^{-1}$. Note that $\sigma_0$ is usually corrected to a circular aperture with diameter $1.19\,h^{-1}$ kpc, corresponding to a radial range $\sim 0.05\,R_e$–$R_e$ for $h = 0.5$, and for typical values of $R_e$ (e.g., Jørgensen et al. 1995).

In addition, for a stationary stellar system the scalar virial theorem can be written as

$$\frac{G\Upsilon_* L}{R_e} = K_V \sigma_0^2, \quad (2)$$

where $\Upsilon_*$ is the *stellar* mass-to-light ratio in the photometric band used for the determination of $L$ and $R_e$, while the coefficient $K_V$ takes into account projection effects, the galaxy stellar density distribution, the stellar orbital distribution (such as velocity dispersion anisotropy and rotational support), and the effects related to the presence of dark matter. Equations (1) and (2) imply that in real galaxies, no matter how complex their structure is, $\Upsilon_*/K_V$ is a well-defined function of any two of the three observables $(L, R_e, \sigma_0)$ and this dependence is commonly referred as the "FP tilt". In other words, the FP tilt indicates that *structural/dynamical* ($K_V$) and *stellar population* ($\Upsilon_*$) properties in real galaxies are strictly connected, possibly as a consequence of their formation process. Overall, the interpretation of the FP cannot be limited to the study of its tilt only, but requires to take consistently into account also its thinness (as done, for example, in the "orthogonal exploration" approach, see Renzini & Ciotti 1993; Ciotti et al. 1996; Ciotti & Lanzoni 1997). A step forward in the study of the structural and dynamical implications of the tilt and thinness of the FP was made by Bertin et al. (2002), who introduced, although limited to spherical models, the more general Monte-Carlo approach. The Monte-Carlo approach was successively applied

by Lanzoni & Ciotti (2003, hereafter LC) to the investigation of projection effects on the FP thickness, by adopting fully analytical axisymmetric one-component Ferrers galaxy models (Ferrers 1877). In particular, LC found that while projection effects do contribute to the observed FP scatter, nonetheless the FP *physical scatter* (as determined by variations of the physical properties from galaxy to galaxy), sums up to 90% of the intrinsic FP scatter. In addition, LC found that the contribution of ordered streaming motions to the observed velocity dispersion is negligible when small/medium apertures ($\lesssim R_e$) are used for the spectroscopic observations. Unfortunately, while fully reliable about projection effects on $R_e$ (which are independent of the specific homeoidal density profile adopted), the central regions of Ferrers models are unrealistically flat, so that doubts can be risen about the use of their central velocity dispersion to estimate streaming velocity effects. Moreover, what is the additional effect of a central super-massive black hole (SMBH) or of a dark matter halo? An attempt to answer the questions above was made by Ciotti & Bertin (2005, hereafter CB) by using fully analytical cuspy galaxy models obtained from a homeoidal expansion, qualitatively confirming the results of LC. Here, in order to extend the results of LC and CB, we numerically solve the Jeans and projected dynamics equations for more realistic, oblate galaxy models with a central cusp, and variable amount of internal streaming velocity, allowing for the presence of a central SMBH and a dark matter halo.

The paper is organized as follows. In Sect. 2 we derive the relevant intrinsic and projected properties of the adopted models, while in Sects. 3–5 we present the main results of our analysis together with some observationally related consequences, such as the model position in the $v/\sigma$-ellipticity plane. In Sect. 6 we summarize the results, while in the Appendix we present the fully analytical model adopted to test the numerical code.

## 2. The models

### 2.1. 3D quantities

At variance with LC, who adopted the centrally flat and spatially truncated Ferrers models, we now use cuspy oblate galaxy models with homeoidal density distribution, belonging to the family of the so-called $\gamma$-models (Dehnen 1993; Dehnen & Gerhard 1994, hereafter DG; Tremaine et al. 1994; Qian et al. 1995). Their density profile is

$$\rho_* = \frac{M_*}{4\pi R_c^3\, q}\,\frac{(3-\gamma)}{m^\gamma\,(1+m)^{4-\gamma}}, \quad (0 \le \gamma < 3), \tag{3}$$

where $M_*$ is the total mass, $R_c$ the characteristic scale, and in cylindrical coordinates[2] $m \equiv \sqrt{\tilde{R}^2 + \tilde{z}^2/q^2}$, with $\tilde{R} \equiv R/R_c$ and $\tilde{z} \equiv z/R_c$; the parameter $0 < q \le 1$ measures the intrinsic model flattening. Note that these models for $\gamma \simeq 0.75$ and $\gamma \simeq 1$ provide a good representation (in the central regions) of the de Vaucouleurs (1948) and of the Navarro et al. (1997, NFW) profiles, respectively. In two-component models the dark matter halo is also described by a density profile as in Eq. (3), in general with a different total mass, scale-radius, density slope and flattening; a SMBH of mass $M_{BH}$ can be also added at the model center. In all cases, the stellar mass-to-light ratio $\Upsilon_*$ is assumed to be constant within each model.

We assume that the density profile in Eq. (3) is supported by a two-integrals distribution function $f(E, L_z)$[3] (where $E$ and $L_z$ are the energy and the $z$-component of the angular momentum of stars per unit mass, respectively), and the Jeans equations are

$$\frac{\partial \rho_* \sigma_R^2}{\partial z} = -\rho_* \frac{\partial \phi}{\partial z}, \tag{4}$$

$$\frac{\partial \rho_* \sigma_R^2}{\partial R} - \frac{\rho_*(\overline{v_\varphi^2} - \sigma_R^2)}{R} = -\rho_* \frac{\partial \phi}{\partial R}, \tag{5}$$

where $\phi$ is the total gravitational potential, $v_R = v_z = 0$, the off-diagonal elements of the velocity dispersion tensor vanish, and $\sigma_R^2 = \sigma_z^2$ (see, e.g., Binney & Tremaine 1987, hereafter BT).

As in LC, $\overline{v_\varphi^2}$ is splitted into streaming motion $v_\varphi^2 \equiv \overline{v}_\varphi^2$ and azimuthal velocity dispersion $\sigma_\varphi^2 \equiv \overline{(v_\varphi - v_\varphi)^2} = \overline{v_\varphi^2} - v_\varphi^2$ with the Satoh (1980) $k$-decomposition:

$$v_\varphi^2 = k^2(\overline{v_\varphi^2} - \sigma_R^2), \tag{6}$$

and

$$\sigma_\varphi^2 = \sigma_R^2 + (1-k^2)(\overline{v_\varphi^2} - \sigma_R^2), \tag{7}$$

with $0 \le k \le 1$. For $k = 0$ no ordered motions are present, and the velocity dispersion tensor is maximally tangentially anisotropic, while for $k = 1$ the velocity dispersion tensor is isotropic, and the galaxy flattening is due to azimuthal streaming velocity (the so-called "isotropic rotator" case).

As well known, the gravitational potential of the density distribution in Eq. (3) cannot be expressed in terms of elementary functions, and so we compute it by using an expansion in orthogonal function: Eqs. (4) and (5) are then integrated numerically (Sect. 2.3).

### 2.2. Projected quantities

In order to project the model properties on the plane of the sky (the projection plane), we define the observer system as a Cartesian coordinate system $(x', y', z')$ with the line-of-sight (*los*) parallel to the $z'$ axis, and with the $x'$ axis coincident with the $x$ axis of the natural Cartesian system introduced in Sect. 2.1. The angle between $z$ and $z'$ is $0 \le \theta \le \pi/2$: $\theta = 0$ corresponds to the face-on view of the galaxy, while $\theta = \pi/2$ to the edge-on view. With this choice, the projection plane is $(x', y')$ and the *los* direction in the natural coordinate system is

[2] The $(R, \varphi, z)$ coordinates are related to the natural Cartesian coordinates by the relations $R = \sqrt{x^2 + y^2}$, $\cos\varphi = x/R$, $\sin\varphi = y/R$. From now on, the symbol "$\sim$" over a coordinate will indicate normalization to $R_c$.

[3] Note that the important issue of the models phase-space consistency is beyond the tasks of this work (see Qian et al. 1995). We use symbol $\mathbf{v}$ for the velocity in the phase space, while $\boldsymbol{v}(\boldsymbol{x}) \equiv \overline{\mathbf{v}}$ is the *streaming* velocity. In general, a bar over a quantity means average over phase-space velocities.

given by $\boldsymbol{n} = (0, -\sin\theta, \cos\theta)$[4]. Following LC we indicate with $\Sigma(\ell)$ the projected (mass or light) density distribution, where

$$\begin{cases} \ell^2 \equiv x'^2 + y'^2/q(\theta)^2, \\ q(\theta)^2 \equiv \cos^2\theta + q^2 \sin^2\theta. \end{cases} \tag{8}$$

The quantity $\ell$ determines the size of the elliptic isophotes, and their *ellipticity* is given by $\varepsilon = 1 - q(\theta)$. For fixed $\ell$ the major and minor isophotal semi-axes are $a = \ell$ and $b = q(\theta)\ell$, and the associated *circularized radius* is defined as $\pi R_\ell^2 = \pi ab$, i.e., $R_\ell = \sqrt{q(\theta)}\ell$. In particular, the *circularized effective radius* is

$$R_\mathrm{e} = \sqrt{q(\theta)}\ell_\mathrm{e}, \tag{9}$$

where $M_\mathrm{p}(\ell_\mathrm{e}) = M/2$, with $M_\mathrm{p}(\ell)$ being the projected mass within $\ell$. Thus the identity $R_\mathrm{e} = \sqrt{q(\theta)}R_\mathrm{e}^0$ (where $R_\mathrm{e}^0$ is the effective radius of the model when seen face–on or in case of spherical symmetry) is a common property of all axisymmetric homeoidal distributions, independently of their specific density profile, and so the dependence on $\theta$ of the circularized effective radius of the present models and those in LC is identical.

The projected velocity fields at $(x', y')$ are obtained by numerical integration of the projection along $\boldsymbol{n}$ of their spatial counterpart. This is done by transforming the corresponding spatial velocity moments from cylindrical to Cartesian coordinates (LC, Eqs. (21)–(27)). Note that, in presence of a non-zero projected streaming velocity field $v_\mathrm{p}$, the velocity dispersion accessible to observation is

$$\begin{aligned} \sigma_\mathrm{los}^2(x', y') &\equiv \frac{1}{\Sigma(\ell)} \int_{-\infty}^{\infty} \rho \, \overline{\left(\langle \mathbf{v}, \boldsymbol{n}\rangle - v_\mathrm{p}\right)^2} \, \mathrm{d}z' \\ &= \sigma_\mathrm{p}^2 + V_\mathrm{p}^2 - v_\mathrm{p}^2, \end{aligned} \tag{10}$$

where $\langle , \rangle$ is the standard inner product, and for the definition of $V_\mathrm{p}^2$ (the *los* integration of $v_\mathrm{n}^2$, i.e. the squared component along $\boldsymbol{n}$ of the streaming velocity field) and of $\sigma_\mathrm{p}^2$ we again refer to LC. Note also that, independently of the *los* orientation, $v_\mathrm{n} = 0$ on the isophotal minor axis $y'$, and thus $\sigma_\mathrm{los}^2 = \sigma_\mathrm{p}^2$ there. In addition, $\sigma_\mathrm{los}^2 = \sigma_\mathrm{p}^2$ everywhere when observing the galaxy face-on ($\theta = 0$), or in the case $k = 0$ (no rotation). Finally, since the observed velocity dispersion is always measured within the aperture of the spectrograph, we integrate $\sigma_\mathrm{los}^2$ over circular apertures of radius $R_\mathrm{a}$:

$$M_\mathrm{p}(R_\mathrm{a})\sigma_\mathrm{a}^2(R_\mathrm{a}) \equiv \int_{R' \le R_\mathrm{a}} \Sigma(x', y')\sigma_\mathrm{los}^2(x', y') \, \mathrm{d}x' \, \mathrm{d}y'. \tag{11}$$

In the following we will identify the quantity $\sigma_0$ appearing in the FP with $\sigma_\mathrm{a}$.

### 2.3. The numerical code

The solution of the Jeans equations and the projection of the density and of the various kinematical quantities are calculated with a grid-based numerical code developed by one of us (AR). The gravitational potential is obtained by solving the Poisson equation $\nabla^2\phi = 4\pi G\rho$ in spherical coordinates $(r, \vartheta, \varphi)$, specializing the Londrillo & Messina (1990) spectral method to axisymmetric systems. The $\vartheta$ (co-latitude) dependence of $\rho$ and $\phi$ is described with standard Legendre polynomials, while the spherical radius is mapped as

$$r \equiv \tan^2(u/2), \qquad (0 \le u \le \pi). \tag{12}$$

The resulting radial $u$-Laplace operator, when acting on Chebyshev polynomials $T_n(\cos u)$, originates a finite linear combination of such orthogonal functions, used to expand the density and the gravitational potential. Equations (4) and (5) are then integrated with a cubic spline algorithm on a logarithmic $(R, z)$ grid, in order to sample the model central regions at high resolution (as required by the density cusp and by the possible presence of a SMBH). Since the projection coordinate system is tilted with respect to the natural coordinate system by an angle $\theta$, the grid points of the two systems in general do not coincide, and so an interpolation and the *los* integrations are performed with a cubic spline algorithm. For obvious symmetry reasons, the computations are restricted to the first quadrant.

The double precision C code is organized in a library of functions, and all the relevant intrinsic and projected fields of each model are computed in ∼100 s on a 1.33 GHz processor, for a $512^3$ grid. The code accuracy has been tested by solving the Poisson, Jeans, and projected equations for the Miyamoto-Nagai (1975) models (see also Ciotti & Pellegrini 1996), for the spherical $\gamma$-models, and for the Ferrers ellipsoids: for these models all the relevant dynamical properties and, to some extent, even the projected fields are known analytically. In addition, we also compared our numerical results with the analytical (asymptotic) models presented in the Appendix and in CB, obtaining relative errors $\lesssim 10^{-3}$ for the intrinsic dynamical properties and $\lesssim 10^{-2}$ for the projected fields (also in the central regions and in presence of a SMBH). Finally, for all models presented in the following section we verify numerically the projected virial theorem

$$2n_i n_j K_{ij} = -n_1^2 W_{11}^2 - n_2^2 W_{22}^2 - n_3^2 W_{33}^2, \tag{13}$$

with $K_{ij}$ and $W_{ij}$ being the kinetic and potential energy tensors (e.g. Ciotti 2000, see also Eqs. (31), (A.8), (A.11), (A.12) in LC).

## 3. General results

Before studying in detail the effect of ordered rotation on the measured velocity dispersion in elliptical galaxies and its consequences on the FP, we present a few representative models in order to illustrate the general properties of their projected kinematical fields (see also DG). In particular, since ordered rotation enters in the definition of $\sigma^2$ through the quantities $v_\mathrm{p}$ and $V_\mathrm{p}$ (Eq. (10) and (11)), and since these quantities are maximized for isotropic rotators seen edge-on, we restrict to this configuration in the following discussion.

In Fig. 1 (top left panel) we show $v_\mathrm{p}$ along the major axis for three different values of the galaxy density inner slope ($\gamma = 0, 1, 1.5$) and two different flattenings ($q = 0.3, 0.8$)

[4] The *los* vector points *toward* the observer, and so *positive* velocities correspond to a *blue-shift*; the general framework for the projection is given in LC.

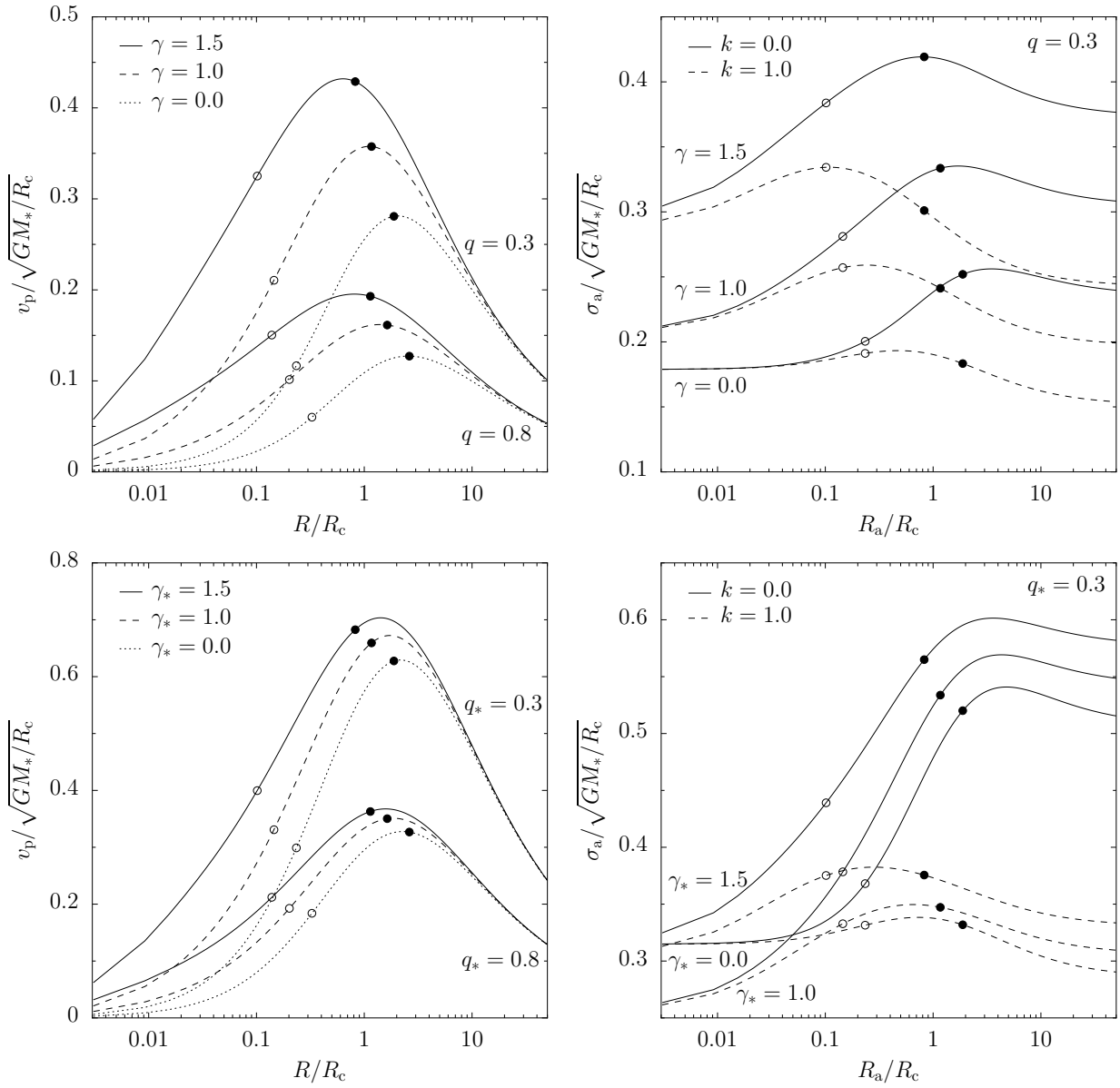


**Fig. 1.** Edge-on, major axis projected streaming velocity $v_p$ (*left panels*), and aperture velocity dispersion $\sigma_a$ (*right panels*) for one (*upper panels*) and two-component (*lower panels*) galaxy models. Projected streaming velocity is shown for isotropic models only, while $\sigma_a$ for isotropic and fully tangentially anisotropic (i.e. not rotating) models. Aperture radii corresponding to $R_e/8$ and $R_e$ are marked as empty dots (∘) and solid dots (•), respectively. In two-component models the dark matter halo is described by a spherical Hernquist (1990) model ($\gamma = 1$, $q = 1$ in Eq. (3)), with $M_h = 5\,M_*$ and $R_h = 2\,R_c$.

in one-component isotropic models without central SMBH. Consistently with Eqs. (A.5) and (6), and with CB (Eq. (C.8)), in central regions $v_p$ vanishes in all the considered cases. The projected streaming velocity also vanishes independently of $\gamma$, as $R \to \infty$, where the density profile $\propto m^{-4}$. The major axis projected streaming velocity thus presents a rapid increase up to a maximum, placed very near to the model circularized effective radius, followed by a mild decrease for increasing radial coordinate (note the logarithmic scale of the $x$-axis). Apparently, at fixed galaxy mass and scale-length, the main parameters determining the projected velocity $v_p$ are the galaxy flattening $q$, and the slope $\gamma$ of the central cusp. In Fig. 1 (top right panel) we show the aperture velocity dispersion $\sigma_a$ for the same models (with $q = 0.3$) in the left panel, either supported by tangential anisotropy ($k = 0$, solid line), or by ordered rotation ($k = 1$, dashed line). In general, $\sigma_a$ is larger for $k = 0$ than for $k = 1$ at any fixed aperture, and this is so because tangential anisotropy is maximal when $k = 0$, while the streaming motions (that are maximal for $k = 1$) contribute to $\sigma_{los}$ with the term $V_p^2 - v_p^2$ which is small (see Eq. (10)). This dependence of $\sigma_a$ on $k$ is explicit in Eq. (29) in CB. In any case, also $\sigma_a$ presents a maximum, which is near $R_e/8$ for the isotropic rotators, and near $R_e$ for non-rotating models.

An important quantitative result of our models is that $\sigma_a$ differs less than 15% between the non-rotating and maximally rotating cases, when $R_a \lesssim R_e/8$ since $v_p$ and $V_p$ vanish near the

galaxy center. When integrating $\sigma_{\rm los}$ over a larger area ($R_{\rm a} \sim R_{\rm e}$), however, the differences between $\sigma_{\rm a}$ of the anisotropy-supported and the rotation-supported models increase for increasing $\gamma$, attaining a value of about 30% in the most extreme case ($\gamma = 1.5$).

In Fig. 1 (bottom panels) we show the same quantities of the corresponding upper panels, for identical galaxy models at which we added a spherically symmetric ($q_h = 1$) dark matter halo with $M_h = 5M_*$ and $R_h = 2R_c$. For the halo central cusp we adopted $\gamma = 1$, in order to mimic the central behavior of the NFW density profile. Qualitatively the results are similar to those of the one-component models, the main effect being the substantial increase of $\sigma_{\rm a}$ for large apertures in the $k = 0$ case. Note also that in the central regions the effect of the adopted dark matter halo is negligible, as revealed by Eqs. (A.4), (A.5) with $M_{\rm BH} = 0$. Analogous results are obtained also with halos with different mass or scale radius.

Compared to the observations (e.g., Mehlert et al. 2000), while the model rotational velocity profiles are quite realistic, the aperture velocity dispersion presents a central dip that seems at odd with what empirically inferred from the data (e.g., Jørgensen et al. 1995; Mehlert et al. 2003; Cappellari et al. 2005). This is an unrealistic, but very well known, feature of several dynamical models with cuspy density distributions, which produce centrally vanishing velocity dispersion profiles (see Eq. (A.4); e.g., Bailey & MacDonald 1981; Dehnen 1993; Tremaine et al. 1994; and Bertin et al. 2002 for a general discussion in the case of spherical symmetry). Such a central dip in the models often occurs at small radii, so that it is undetectable in the data or it nicely agrees with few observed cases (e.g., Graham et al. 1998; Emsellem et al. 2004; Cappellari et al. 2005). This is also what we find for our isotropic rotators, but cannot apply to the case of non-rotating models, which show a peak in the *los* velocity dispersion profile well far from the galaxy center, near the effective radius. However, we stress again that here we are considering the most extreme (thus also possibly unrealistic) cases, in order to maximize the effects of ordered rotation, while these unobserved features become much weaker for milder flattenings, intermediate *los* inclinations, and non-zero rotational support. We therefore consider our results reliable and conclude that the contribution of the rotational velocity to the *observed* central velocity dispersion ($R_{\rm a} \lesssim R_{\rm e}/8$) is usually negligible for elliptical galaxies in the local Universe, also in presence of a cuspy dark matter halo. This implies, that *a systematic increase of rotational support with decreasing galaxy luminosity is not at the origin of the tilt of the FP of elliptical galaxies* (see also Busarello et al. 1997, LC). However, our results also suggest that particular care should be used when constructing the FP of galaxies at high redshift (where spectroscopic apertures usually enclose a large fraction of the galaxy). In fact, the increasing difference of $\sigma_{\rm a}$ between rotating and non rotating galaxies, with increasing $R_{\rm a}$ (dashed line in Fig. 1) would lead, if not properly taken into account, to underestimate the galaxy mass (when interpreting $\sigma_{\rm a}$ by means of virial estimators based on spherical, not rotating models) up to 70% for low-mass and rotating objects (see also Bender et al. 1992; van Albada et al. 1995). These aperture effects might so contribute (in part) to the observed decrease of the mass-to-light ratio of low-mass galaxies at high redshift (e.g., di Serego Alighieri et al. 2005; Treu et al. 2005; van der Wel et al. 2005).

### 3.1. Effects of a central super-massive black hole

It is now commonly accepted that SMBHs reside in the center of stellar spheroids, and that their mass $M_{\rm BH}$ scales almost linearly with the stellar mass of the parent galaxy, with $M_{\rm BH}/M_* \approx 10^{-3}$ (Magorrian et al. 1998). An order-of-magnitude estimate of the radius $r_{\rm BH}$ of the "sphere of influence" (i.e., the region within which the gravitational effects of the SMBH on the stellar orbits are significant) is usually obtained as $GM_{\rm BH}/r_{\rm BH} = 3\,\sigma_*^2/2 \approx GM_*/(2\,r_{\rm vir})$, i.e., $r_{\rm BH}/R_{\rm e} \approx 6 \times 10^{-3}$ (where $\sigma_*$ is the one-dimensional stellar velocity dispersion, and $r_{\rm vir}/R_{\rm e} \simeq 2.97$ for a $R^{1/4}$ galaxy; see Ciotti 1991). Thus, SMBH effects should be detectable on scales of few parsecs or tens of parsecs only, in any case well within the standard central aperture of $R_{\rm e}/8$. However, while in galaxy models without SMBH $v_\varphi$ and $v_{\rm p}$ vanish at the center for $\gamma < 2$, in presence of a SMBH $v_\varphi^{\rm BH} \propto v_{\rm p}^{\rm BH} \propto 1/\sqrt{R}$, and in principle even an unresolved but luminosity weighted, central kinematical spike could produce detectable effects on $\sigma_{\rm a}$. The results obtained with our models are illustrated in Fig. 2 (left panel), where we show the spatial and projected streaming velocity along the major axis of an isotropic $\gamma = 1$ model with $q = 0.3$ and with a central SMBH having $M_{\rm BH}/M_* = 10^{-3}$. It can be seen that while $v_\varphi$ increases by nearly one order of magnitude in the innermost regions, $v_{\rm p}$ (the only one directly accessible to observations) is much less affected by the presence of the SMBH. Note that from Eq. (A.5), and CB (Eq. (C.8)), $v_\varphi^{\rm BH}/v_\varphi \propto v_{\rm p}^{\rm BH}/v_{\rm p} \propto R^{(\gamma-3)/2}$. In all explored models we found that the SMBH influence is negligible for $R \gtrsim R_{\rm e}/8$.

In Fig. 2 (right panel) we show for the same model the intrinsic one-dimensional and *los* velocity dispersions along the major axis, and the aperture velocity dispersion as a function of $R_{\rm a}$. Note that from Eq. (A.4) and Eqs. (C.3), (29)-(30) of CB we expect $\sigma_R^{\rm BH}/\sigma_R \propto \sigma_{\rm los}^{\rm BH}/\sigma_{\rm los} \propto \sigma_{\rm a}^{\rm BH}/\sigma_{\rm a} \propto R^{(\gamma-3)/2}$. In fact, our numerical results confirm this radial trend, and also show that the SMBH influence decreases along the sequence $\sigma_z$, $\sigma_{\rm los}$ and $\sigma_{\rm a}$ at fixed radial coordinate. A comparison of the two panels in Fig. 2 shows that velocity dispersions are less affected than rotational velocities by the presence of a central SMBH. We thus conclude, that, in general, the presence of a SMBH can be neglected when using the measured "central" ($R_{\rm a} \simeq R_{\rm e}/8$) velocity dispersion, for the construction of the Faber-Jackson (1976), FP, and $M_{\rm BH}$-$\sigma$ relations (Ferrarese & Merritt 2000; Gebhardt et al. 2000), as well as the $v/\sigma$-ellipticity plane (Illingworth 1977; Binney 1978). Accordingly, in the following Sections we will not consider a central black hole in the models.

## 4. Contribution of rotational velocity to the FP thickness

In a follow-up of LC we now investigate the contribution of projection and ordered rotation on the observed FP thickness. As anticipated in the Introduction, the only differences with respect to the results of LC are possibly due to the new value

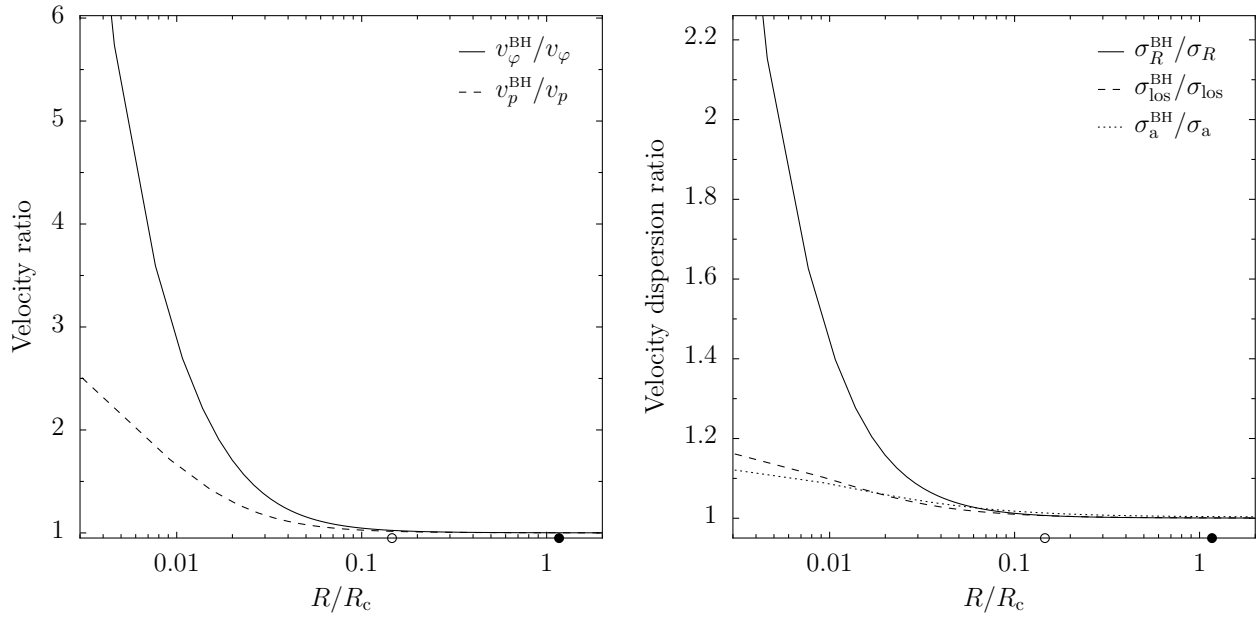


**Fig. 2.** *Left panel*: intrinsic (solid line) and projected (dashed line) streaming velocities on the equatorial plane ($z = 0$) of a model with $\gamma = 1$, $q = 0.3$, $k = 1$, and a SMBH with $M_{\rm BH} = 10^{-3}\,M_*$ normalized to the corresponding quantity of the same model without the SMBH. *Right panel*: intrinsic (solid line), line-of-sight (dashed line), and aperture velocity dispersion ratios (dotted line) for the same model. The aperture velocity dispersion is calculated for a circular aperture $R_{\rm a} = R$. The empty (○) and solid (●) dots correspond to $R_{\rm e}/8$ and $R_{\rm e}$, respectively.

of $\sigma_0$, since the variations of the circularized effective radius $R_{\rm e}$ (and of $I_{\rm e}$) are independent of the specific stellar density profile adopted (provided it is stratified on similar ellipsoids). We start by illustrating how models "move" in the edge-on view of the FP as a function of their intrinsic ($\gamma$, $q$, $k$) and observational ($\theta$) parameters. In Fig. 3 (left panel) we show the edge-on view of the FP of Coma cluster ellipticals as given by Eq. (1) (solid line), and its rms scatter ≃0.057 (dashed line, as obtained by JFK for galaxies with $\sigma_0 \geq 100$ km s$^{-1}$, and after correction for measurement errors). The three families of models superimposed are determined (from top to bottom) by ($q$, $k$) = (0.3, 0), (0.3, 1), and (0.6, 1). For simplicity, $\gamma = 1$ in all models, while three different aperture radii $R_{\rm a}$ are considered to measure $\sigma_0 = \sigma_{\rm a}$, namely $R_{\rm a} = R_{\rm e}/8$ (dots), $R_{\rm e}$ (squares), $10\,R_{\rm e}$ (triangles). The cases corresponding to $\theta = 0$ and $R_{\rm a} = R_{\rm e}$ are arbitrarily placed on the FP best-fit line, and the displacements correspond to $\theta$ increasing from 0 to $\pi/2$. According to Eq. (8), when the *los* inclination changes from 0 to $\pi/2$, $R_{\rm e}$ decreases (and $I_{\rm e}$ increases), thus producing a vertical down-shifts towards the left of the representative models; as expected, displacements are smaller for rounder systems. The additional effect of rotational velocity produces horizontal displacements which depend mainly on the adopted $R_{\rm a}$. For $k = 1$ (isotropic rotators), the variation of $\sigma_{\rm a}$ with the viewing angle $\theta$ is only slightly dependent on the considered spectroscopic aperture, so that the model displacements are almost parallel to each other, but not to the FP. On the contrary, the displacements of non-rotating anisotropic galaxies change considerably both in magnitude and direction as function of $R_{\rm a}$. We have verified that these results are almost independent of the model central cusp $\gamma$. Thus, *due to projection effects, galaxies move in directions which are not exactly parallel to the edge-on FP, but the entity of these displacements is small enough to always maintain the models within the observed FP thickness*. A comparison with Fig. 5 in LC reveals remarkably similar behaviors.

We now restrict the analysis to rotational effects as a function of density slope and galaxy flattening, and in Fig. 3 (right panel) we plot a selection of representative models. As in the left panel, we consider the edge-on view of the FP, and we describe how models "move" when varying the relative amount of rotational and anisotropy support. In particular we show the behavior of three families of models seen edge-on, with different central cusp slopes ($\gamma = 0$, 1, 1.5), and with different flattening $q$. Isotropic models ($k = 1$) are arbitrarily placed on the FP best-fit line. A reduction of the amount of rotational support to zero "moves" models toward the right, placing them at the intermediate points, corresponding to $k = 0$ and $q = 0.6$. More flattened models move even further, until the rightmost points, that represent models with $k = 0$ and $q = 0.3$. These displacements are due to the increasing values of the central velocity dispersion $\sigma_0$ as the rotational support becomes negligible, and their amount increases with both the aperture radius and the galaxy flattening, while it is almost independent of the shape of the central cusp $\gamma$, in agreement with Fig. 1. Note that a preliminary analysis of this problem was given by CB, who adopted homeoidal expansion to investigate the behavior of the projected velocity dispersion in cuspy oblate models with a central SMBH. A comparison of our results with Fig. 2 of CB and results discussed therein, reveals very similar behaviors. Note that the models showed in Fig. 3 (right panel) are all observed edge-on, in order to maximize the rotation effect; when all the possible line-of-sight and the distribution of intrinsic ellipticities are taken into account (as in the Monte-Carlo approach in LC) the statistical displacements would be essentially negligible.

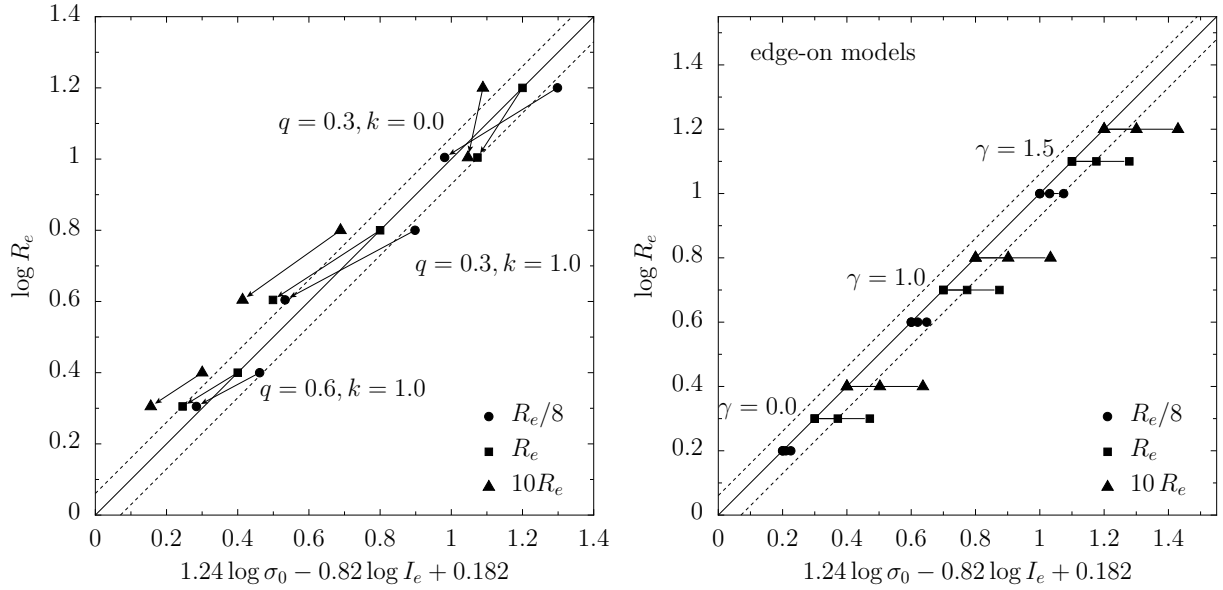


**Fig. 3.** *Left panel*: projection effects on the galaxy models in the space where the FP for Coma cluster galaxies is seen edge-on (solid line) with 1-rms scatter (dashed line) from JFK. The intrinsic model parameters are given by labels, and $\gamma = 1$ for all models. For each model three spectroscopic apertures for $\sigma_a = \sigma_0$ are considered ($R_e/8$: dots, $R_e$: square, $10R_e$: triangles). The *los* inclination increases from $\theta = 0$ (face-on) to $\theta = \pi/2$ (edge-on) along the arrows, and the cases $\theta = 0$, $R_a = R_e$ are *arbitrarily* placed on the FP best-fit line. *Right panel*: maximum rotational effects as a function of intrinsic flattening and spectroscopic aperture $R_a$ for three edge-on models ($\gamma = 0$, 1, 1.5). The isotropic rotators with $q = 0.6$ are *arbitrarily* placed on the FP while, on each horizontal line, the middle points correspond to models with $k = 0$ and $q = 0.6$, while the rightmost points to models with $k = 0$ and $q = 0.3$.

From the study of the models presented in this section, and from their comparison with models in LC and CB we then confirm and extend the conclusions of LC to cuspy galaxies, *i.e. that projection effects only marginally contribute to the FP thickness,* 90% *of it being due to variations, from galaxy to galaxy, of their intrinsic physical properties*. In particular, we proved that variations of rotational support from galaxy to galaxy *only marginally contribute to the FP thickness*.

## 5. The $v/\sigma$-ellipticity plane

With the aid of the developed models we finally study how the $v/\sigma$-ellipticity plane (an important tool used to investigate to what extent the galaxy flattening is due to velocity dispersion anisotropy, e.g. see Illingworth 1977; Binney 1978) is populated by galaxies as a function of the adopted aperture $R_a$ and of their streaming velocity support. Traditionally, observational data are the peak projected streaming velocity $v_{p,max}$ a "central" aperture velocity dispersion $\sigma_0$, and galaxy ellipticity. Data points are then compared with the family of curves obtained from the tensor virial theorem, where $v^2$ and $\sigma^2$ are the mass weighted square streaming velocity and velocity dispersion computed over the whole galaxy. As well known, the tensor virial theorem predictions are independent of the specific galaxy density profile as far as it is homeoidally stratified (Roberts 1962). For example, the thick solid line I in Fig. 4 is obtained from Eq. (4.95) of BT (see also Eq. (9) of Binney 2005), and corresponds to isotropic rotators seen edge-on. Galaxies whose representative points lie significantly below this curve are considered anisotropy supported. Unfortunately it is not straightforward to connect the virial quantities to the observable ones. For this reason, the tensor virial theorem curves are often "corrected" to take into account projection

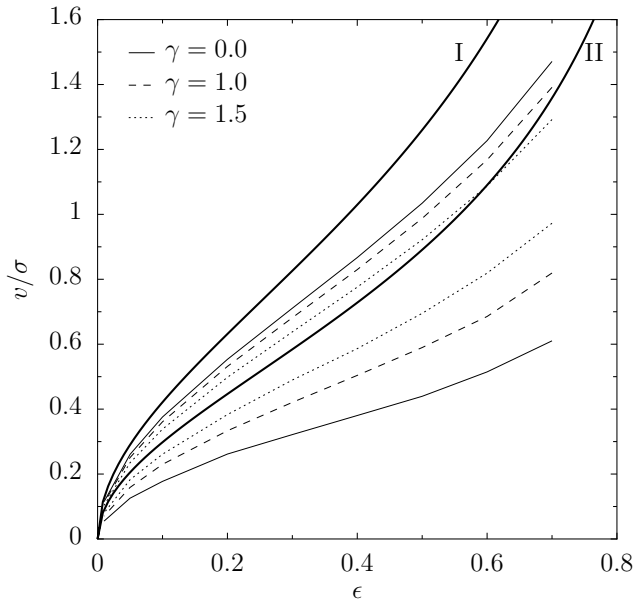


**Fig. 4.** Rotational parameter for isotropic, edge-on models as a function of their ellipticity. The solid thick curve I is the locus of isotropic, classical ellipsoids as obtained from the tensor virial theorem (Binney 1978; see also Eq. (4.95) in BT), while solid line II is derived from the sky-averaged tensor virial theorem (Eq. (26) of Binney (2005), with $\delta = 0$ and $\alpha = 0$) . The upper set of curves represents our models when $v_p = v_{p,max}$, while the lower set of curves represents our models when $v = v_p(R_e/8)$. In all cases we adopt $\sigma = \sigma_a(R_e/8)$.

effects, and in general these corrections makes curve I flatter (e.g., see Eq. (4.5) and Figs. 8 and 9 in Evans & de Zeeuw 1994, and Figs. 4.5 and 4.6 in BT). The situation became even more complicate when Evans & de Zeeuw (1994) showed that $v/\sigma$ for their nearly isotropic "power-law" galaxy models, not only was systematically below curve I of classical spheroids (and significantly so at large ellipticities), but also below the "corrected" locus. Of course, this behavior is not unexpected because, as discussed by Evans & de Zeeuw (1994), the density of their model is not stratified on ellipsoidal surfaces. In addition, their projected streaming velocity does not have a maximum, and its fiducial value must therefore be taken at some arbitrary distance from the center. Interestingly, a very similar behavior is also shown by the isotropic models described in CB (Fig. 2): in this case, due to the models scale-free nature, $v_{\rm p}$ and $\sigma_{\rm a}$ adopted to construct $v/\sigma$ were taken at the same radius.

Fortunately, it is now possible to observationally map the rotation speed and the velocity dispersion over a substantial fraction of a galaxy's image (e.g. the SAURON project, see de Zeeuw et al. 2002; Cappellari et al. 2005). Thus, one can use the sky-averaged quantities to define $v/\sigma$, and predict its trend from the projected virial theorem (e.g. Binney 2005, see also Ciotti 1994, 2000). Curve II in Fig. 4 shows the corresponding locus of the edge-on isotropic rotators, as given by Binney (2005).

Here we use our (isotropic, edge-on, and homeoidally stratified) models to study the effects of light profile central cusps and different definitions of the projected streaming velocity, in determining the model position in the $v/\sigma$-$\epsilon$ plane, while for simplicity we fix $\sigma = \sigma_{\rm a}(R_{\rm e}/8)$. In particular, we consider the cases $v = v_{\rm p,max}$ (the maximum projected velocity) and $v = v_{\rm p}(R_{\rm e}/8)$, as representative of the measured rotation. The resulting trends are shown in Fig. 4, and it is clear how *all the resulting curves lie below the (uncorrected) locus of isotropic, classical ellipsoids obtained from the tensor virial theorem (solid line* I*)*. Deviations with respect to the "classical" expectation are larger when $v = v_{\rm p}(R_{\rm e}/8)$, a case analogous to those considered by CB. Remarkably, our analysis shows that *curve* II (derived from the sky-averaged virial theorem) *provides a much better estimate of $v/\sigma$ (and so, of anisotropy) than the original one based on the (unprojected) tensor virial theorem, when $\sigma = \sigma_{\rm a}(R_{\rm e}/8)$ and $v = v_{\rm p,max}$*. Note also how the central cusp slope can be important, especially when using small aperture to determine $v$.

Thus we conclude that particular care should be placed on the choice of the theoretical $v/\sigma$ locus to be used for comparison with the data, as a function of the quality and extension of the data themselves (see also DG).

## 6. Discussion and conclusions

In this paper we have quantified the contribution of ordered rotation to the FP tilt and thickness. We adopted a class of oblate galaxy models with central cusp and adjustable flattening and amount of rotational support. We also considered models with a dark matter halo and with a central super-massive black hole. The associated Jeans equations have been (numerically) solved under the assumption of an underlying two-integrals distribution function. The main results can be summarized as follow:

1. For the adopted family of models the effect of a central SMBH is stronger on streaming velocities than on velocity dispersions. However, for mass ratios of the order of those predicted by the Magorrian relation, the effect is in general negligible, and the presence of a central SMBH can be neglected when studying relations such as the FP.
2. In agreement with previous results of LC and CB, also for the adopted class of cuspy models the contribution of streaming motions to the observed velocity dispersion is negligible when small/medium apertures ($\lesssim R_{\rm e}$) are used for the spectroscopic observations. This implies that a systematic decrease of rotational support with increasing luminosity *is not* at the origin of the tilt of the FP of elliptical galaxies at low-redshift.
3. In general, the aperture velocity dispersion measured at $R_{\rm a} \gtrsim R_{\rm e}$ is larger for not rotating models than for rotationally supported models (and the difference increases significantly when a dark matter halo is present). This must be taken properly into account when studying the FP, or estimating the mass-to-light ratios at high redshift.
4. When observed from different *los* inclinations, models move in the ($\log R_{\rm e}$, $\log I_{\rm e}$, $\log \sigma_0$) space along directions that are not parallel to the edge-on view of the FP, thus confirming that projection effects do contribute to the observed FP scatter. The models displacement depends mainly on their intrinsic flattening (being larger for more flattened systems), on the amount of rotational support, and on the aperture used to measure $\sigma_0$. These effects however, when weighted over the distribution of ellipticities and *los* inclinations, would produce statistical displacements well within the FP thickness, in agreement with the conclusions of LC.
5. Finally, as a by-product of the present investigation we studied the position of the models in the $v/\sigma$-ellipticity plane, a tool used to discriminate between rotationally and velocity dispersion supported galaxies. We found that, while our models remain well below the (uncorrected) locus of classical ellipsoids as determined from the tensor virial theorem, their position is well predicted by sky-averaged projected virial theorem (Binney 2005) if the peak rotational velocity is used.

*Acknowledgements.* We thank Pasquale Londrillo for advice on the numerical code, and the anonymous referee for useful comments. B.L. is supported by a INAF post-doctoral fellowship, and L.C. by the Italian Cofin "Collective phenomena in the dynamics of galaxies".

## Appendix A: A simple, analytical, cuspy and axisymmetric galaxy model with dark matter halo and central SMBH

We present here the internal kinematical fields of a family of power-law galaxy models (constructed with a homeoidal expansion following CB) with dark matter halo and central black hole. The seed distributions for stars and dark matter are $\rho_* = \rho_{*0}/m_*^{\gamma}$ and $\rho_h = \rho_{h0}/m_h^{\delta}$, where $m_*^2 = \tilde{R}^2 + \tilde{z}^2/(1-\epsilon)^2$,

$m_{\rm h}^2 = \tilde{R}^2 + \tilde{z}^2/(1-\eta)^2$ and, without loss of generality, the scale-length of both distributions is $R_{\rm c}$, with $\widetilde{R} \equiv R/R_{\rm c}$ and $\widetilde{z} \equiv z/R_{\rm c}$. According to CB (Eq. (A.2)), the (unconstrained) density and potential expansion are performed for $\gamma\epsilon \leq 1$, $\delta\eta \leq 1$ (with $\gamma$, $\delta > 1$). Thus, from CB (Eq. (26)), the model stellar density distribution and the total potential are

$$\widetilde{\rho}_* = \frac{1-\gamma\epsilon}{\tilde{r}^{\gamma}} + \frac{\gamma\epsilon\tilde{R}^2}{\tilde{r}^{\gamma+2}} \tag{A.1}$$

$$\widetilde{\phi} = \widetilde{\phi}_* + \mathcal{R}\widetilde{\phi}_h - \frac{\mu}{\tilde{r}}, \tag{A.2}$$

where the density is normalized to $\rho_{0*}$, the gravitational potentials to $4\pi G\rho_{*0}R_{\rm c}^2$, $\mu \equiv M_{\rm BH}/4\pi\rho_{*0}R_{\rm c}^3$, and finally $\mathcal{R} \equiv \rho_{h0}/\rho_{*0}$. The explicit expression for $\widetilde{\phi}_*$ and $\widetilde{\phi}_h$ is given in CB (Eq. (27)), and the model (dimensionless) circular velocity is

$$\widetilde{v}_{\rm c}^2 = \frac{5-\gamma-2\epsilon}{(5-\gamma)(3-\gamma)\widetilde{R}^{\gamma-2}} + \mathcal{R}\frac{5-\delta-2\eta}{(5-\delta)(3-\delta)\widetilde{R}^{\delta-2}} + \frac{\mu}{\widetilde{R}}. \tag{A.3}$$

The Jeans equations for the stellar component are integrated following CB [Eqs. (14), (15)], retaining only first order terms in the flattenings $\epsilon$ and $\eta$:

$$\begin{aligned}\widetilde{\rho}_*\sigma_R^2 = {} & \frac{\widetilde{r}^{2(1-\gamma)}}{(5-\gamma)(3-\gamma)}\left[\frac{5-\gamma-4\epsilon}{2(\gamma-1)} - \frac{(4-\gamma)\epsilon\widetilde{z}^2}{\widetilde{r}^2}\right] \\ & + \frac{\mathcal{R}\widetilde{r}^{2-\gamma-\delta}}{(5-\delta)(3-\delta)} \\ & \times\left[\frac{(5-\delta)(1-\gamma\epsilon) - (4-\delta)(\delta-1)\eta}{\gamma+\delta-2}\right. \\ & \left. + \frac{(5-\delta)\gamma\epsilon + (3-\delta)\delta\eta}{\gamma+\delta}\frac{\widetilde{R}^2}{\widetilde{r}^2}\right] \\ & + \frac{\mu}{(3+\gamma)\widetilde{r}^{1+\gamma}}\left(\frac{3+\gamma-2\gamma\epsilon}{1+\gamma} - \frac{\gamma\epsilon\widetilde{z}^2}{\widetilde{r}^2}\right)\end{aligned} \tag{A.4}$$

$$\begin{aligned}\widetilde{\rho}_*\left(\overline{\mathrm{v}_\varphi^2} - \sigma_R^2\right) = {} & \frac{2\epsilon\widetilde{R}^2}{(5-\gamma)(3-\gamma)\widetilde{r}^{2\gamma}} \\ & + \mathcal{R}\frac{2\gamma\widetilde{R}^2}{\widetilde{r}^{\gamma+\delta}}\frac{\epsilon(5-\delta) - \eta(3-\delta)}{(5-\delta)(3-\delta)(\gamma+\delta)} \\ & + \mu\frac{2\gamma\epsilon\widetilde{R}^2}{(3+\gamma)\widetilde{r}^{3+\gamma}}.\end{aligned} \tag{A.5}$$

## References


Bailey, M. E., & MacDonald, J. 1981, MNRAS, 194, 195
Bender, R., Burstein, D., Faber S. M. 1992, ApJ, 399, 462
Bertin, G., Ciotti, L., Del Principe, M. 2002, A&A, 386, 149
Binney, J. 1978, MNRAS, 183, 501
Binney, J., & Tremaine, S. 1987, Galactic Dynamics, (Princeton University Press) (BT)
Binney, J. 2005, MNRAS, submitted [arXiv:astro-ph/0504387]
Busarello, G., Capaccioli, M., Capozziello, S., et al. 1997, A&A, 320, 415
Cappellari, M., Bacon, R., Bureau, M., et al. 2005, MNRAS, submitted [arXiv:astro-ph/0505042]
Ciotti, L. 1991, A&A, 249, 99
Ciotti, L. 1994, CeMDA, 60, 401
Ciotti, L. 2000, Lecture Notes on Stellar Dynamics, (Pisa, Italy: Scuola Normale Superiore editor)
Ciotti, L., & Pellegrini, S. 1996, MNRAS, 279, 240
Ciotti, L., & Lanzoni, B. 1997, A&A, 321, 724
Ciotti, L., & Bertin G. 2005, A&A, 437, 419 (CB)
Ciotti, L., Lanzoni, B., & Renzini, A. 1996, MNRAS, 282, 1
Dehnen, W. 1993, MNRAS, 265, 250
Dehnen, W., & Gerhard, O. E. 1994, MNRAS, 268, 1019 (DG)
de Vaucouleurs, G. 1948, Annales d'Astrophysique 11, 247
de Zeeuw, P. T., Bureau, M., Emsellem, E., et al. 2002, MNRAS, 329, 513
di Serego Alighieri, S., Vernet, J., Cimatti, A., et al. 2005, A&A, accepted [arXiv:astro-ph/0506655]
Djorgovski, S., & Davis, M. 1987, ApJ, 313, 59
Dressler, A., Lynden-Bell, D., Burstein D., et al. 1987, ApJ, 313, 42
Emsellem, E., Cappellari, M., Peletier, R. F., et al. 2004, MNRAS, 352, 721
Evans, N. W., & de Zeeuw, P. T. 1994, MNRAS, 271, 202
Faber, S. M., & Jackson R. E. 1976, ApJ, 204, 668
Faber, S. M., Dressler, A., Davies, R. L., et al. 1987, in Nearly normal galaxies, ed. S. M. Faber (New York: Springer), 175
Ferrarese, L., & Merritt, D. 2000, ApJ, 539, L9
Ferrers, N. M. 1877, Quart. J. Pure Appl. Math., 14, 1
Gebhardt, K., Bender, R., Bower, G., et al. 2000, ApJ, 539, 13
Graham, A. W., Colless, M. M., Busarello, G., et al. 1998, A&AS, 133, 325
Hernquist, L. 1990, ApJ, 356, 359
Illingworth, G. 1977, ApJ, 218L, 43
Jørgensen, I., Franx, M., & Kjærgaard, P. 1995, MNRAS, 276, 1341
Jørgensen, I., Franx, M., & Kjærgaard, P. 1996, MNRAS, 280, 167 (JFK)
Lanzoni, B., & Ciotti, L. 2003, A&A, 404, 819 (LC)
Londrillo, P., & Messina, A. 1990, MNRAS, 242, 595
Magorrian, J., Tremaine, S., Richstone, D. O., et al. 1998, AJ, 115, 2285
Mehlert, D., Saglia, R. P., Bender, R., et al. 2000, A&AS, 141, 449
Mehlert, D., Thomas, D., Saglia, R. P., et al. 2003, A&A, 407, 423
Miyamoto, M., & Nagai, R. 1975, PASJ 27, 533
Navarro J. F., Frenk C. S., & White S. D. M. 1997, ApJ, 490, 493 (NFW)
Pahre, M. A., de Carvalho, R. R., & Djorgovski, S. G. 1998, AJ, 116, 1606
Qian, E. E., de Zeeuw, P. T., van der Marel, R. P., & Hunter, C. 1995, MNRAS, 274, 602
Renzini, A., & Ciotti, L. 1993, ApJ, 416, L49
Roberts, P. H. 1962, ApJ, 136, 1108
Satoh, C. 1980, PASJ, 32, 41
Scodeggio, M., Gavazzi, G., Belsole, E., et al. 1998, MNRAS, 301, 1001
Tremaine, S., Richstone, D. O., Byun, Y., et al. 1994, AJ, 107, 634
Treu, T., Ellis, R. S., Liao, T. X., & van Dokkum, P. G. 2005, ApJ, 622, L5
van Albada, T. S., Bertin, G., Stiavelli, M. 1995, MNRAS, 276, 1255
van der Wel, A., Franx, M., van Dokkum, P. G., et al. 2005, ApJ, accepted [arXiv:astro-ph/0502228]